

# Control structure design of a solid oxide fuel cell and molten carbonate fuel cell integrated system: Bottom-up analysis

Prathak Jienkulsawad<sup>a</sup>, Sigurd Skogestad<sup>b</sup>, Amornchai Arpornwichanop<sup>a,c,\*</sup>

<sup>a</sup> Center of Excellence in Process and Energy Systems Engineering, Department of Chemical Engineering, Faculty of Engineering, Chulalongkorn University, Bangkok 10330, Thailand

<sup>b</sup> Department of Chemical Engineering, Norwegian University of Science and Technology, N-7491 Trondheim, Norway

<sup>c</sup> Bio-Circular-Green-economy Technology & Engineering Center, Department of Chemical Engineering, Faculty of Engineering, Chulalongkorn University, Bangkok, 10330, Thailand

## ARTICLE INFO

### Keywords:

Solid oxide fuel cell  
Molten carbonate fuel cell  
Integrated system  
Control structure design  
Bottom-up analysis

## ABSTRACT

A solid oxide fuel cell and molten carbonate fuel cell integrated system is a power generation system with enhanced fuel and carbon dioxide utilization. Due to its complex structure, designing a control system is important for its smooth and efficient operation. This study is a continuation from the previous study focusing on a top-down, steady-state economic analysis for synthesizing the control structure of the solid oxide fuel cell and molten carbonate fuel cell integrated system to maximize power generation and carbon dioxide utilization. In this study, a bottom-up analysis is performed to design a control layer and validate the proposed control structure via dynamic simulation. The control configuration uses a decentralized approach with proportional-integral-derivative control to maintain the fuel cell system at its optimum target. The control performance with the proposed control structure and configurations are evaluated and analyzed. Four control loops involving gas concentrations are considered, based on different time scales between the regulatory control and supervisory layers. The results of the proposed control system confirm that the integrated fuel cell system is controllable despite the deviation of the fuel cell voltages from their nominal values.

## 1. Introduction

Solid oxide fuel cell (SOFC) is considered as an alternative, reliable power device to replace combustion-based power generators [1]. It provides high energy conversion efficiency, low environmental impact, adequate fuel flexibility, and the possibility for combined heat and power generation with a wide range of applications [2]. As an example of a small application, a SOFC system combined with adsorption and hybrid chillers was applied to a telecommunication system providing the electrical (< 10 kW) and cooling (< 20 kW) energy to a base transceiver station and data center, and the energy savings were about 110 MWh per year compared to a traditional system [3]. The SOFC was also considered as a power generation in the trigeneration system for an educational building with 900 m<sup>2</sup> and 120 kW requirement, giving an overall efficiency of 60% [4]. In addition, the SOFC can act as a fuel reformer with a direct natural gas fuel feed. The reformed gas from the SOFC can further be used in the downstream process for power generation, which can improve the overall energy efficiency by 16% when integrated with a proton exchange membrane fuel cell (PEMFC) [5].

The SOFC system integrated with a solid oxide electrolyser was employed in the industrial facilities of the paper mill and can enhance energy generation efficiency by 6% [6]. Besides stationary applications, SOFCs can be used in the transportation sector. Bessekon et al. [7] showed that a driving range of the SOFC-battery electrical vehicle using a Nissan Leaf Acenta module fed by compressed natural gas, liquefied natural gas, and liquefied petroleum gas can be enhanced by 94 km, 535 km and 653 km, respectively, compared to the original electrical vehicle.

Regarding the power generation system, there are many possible integrated systems with SOFCs. For example, a SOFC integrated with a homogeneous charge compression ignition engine can enhance the electrical efficiency to 59% [8], a SOFC integrated with a gas turbine (GT) and steam turbine has yielded a promising overall energy efficiency of 66.8% [9], and a SOFC integrated with a PEMFC with the gas processing subsystem consisting of a water gas shift reactor and thermal swing adsorption has provided an overall energy efficiency of 64% [10]. Integrated systems are of interest as fuel cannot be used fully by the SOFC itself and can be used for additional power or heat generation.

\* Corresponding author.

E-mail address: [Amornchai.a@chula.ac.th](mailto:Amornchai.a@chula.ac.th) (A. Arpornwichanop).

Nomenclature			
<i>Symbols</i>		$\epsilon$	emissivity (-)
$A$	Area of reaction ( $m^2$ )	$\eta$	voltage loss (V)
$C_p$	Heat capacity ( $J mol^{-1} K^{-1}$ , $kJ kg^{-1} K^{-1}$ )	$\theta$	time delay
$CEC$	Carbon emission coefficient ( $kg CO_2 MWh^{-1}$ )	$\mathfrak{R}$	Gas constant ( $kJ mol^{-1} K^{-1}$ )
$D_h$	Hydraulic diameter (m)	$\sigma$	Stefan-Boltzmann constant ( $W m^{-2} K^{-4}$ )
$E$	Operating voltage (V)	$\sigma_i$	Electronical conductivity ( $ohm^{-1} m^{-1}$ )
$E_{OCV}$	Open-circuit voltage (V)	$\tau_1$	time constant
$E^0$	OCV at standard temperature and pressure (V)	$\tau_2$	second-order lag time constant
$F_i$	Mole flow rate ( $mol s^{-1}$ )	$\tau_i$	Thickness of layer $i$ (m)
$F$	Faraday's constant ( $C mol^{-1}$ )	<i>Subscripts</i>	
$H$	Enthalpy flow (kW)	$a$	Air channel
$I$	Current (A)	$an$	Anode
$j$	Current density ( $A m^{-2}$ )	$B$	Afterburner
$j_0$	Exchange-current density ( $A m^{-2}$ )	$ca$	Cathode
$k$	Thermal conductivity ( $kW m^{-1} K^{-1}$ )	$el$	Electrolyte
$\dot{m}$	Mass flow rate ( $mol s^{-1}$ )	$f$	Fuel channel
$N_i$	Mole of component $i$ (mol)	$I$	Interconnect
$Nu$	Nusselt number (-)	$i$	Gas species
$P_i$	Pressure (atm)	$M$	MCFC
$P_w$	Power (W)	$P$	PEN
$Q$	Heat (kW)	$R$	Reformer
$\hat{R}$	Rate of reaction per area ( $mol m^{-2} s^{-1}$ )	$S$	SOFC
$R$	Rate of reaction ( $mol s^{-1}$ )	$TPB$	Three-phase boundaries
$T$	Temperature (K)	0	Inlet
$U_f$	fuel utilization (%)	<i>Superscripts</i>	
$V$	Volume ( $m^3$ )	$SP$	Setpoint
$y_i$	Molar fraction (-)		
<i>Greek symbols</i>			
$\alpha$	transfer coefficient (-)		

Jienkulsawad et al. [11] proposed the integration of two high-temperature fuel cells, SOFC and MCFC, to enhance fuel and carbon dioxide utilization, providing an electrical efficiency of 57.1%. By integrating SOFC with MCFC, the nickel oxide (NiO) formation on the anode of the SOFC [12], decreasing the catalytic activity due to hydrogen deficiency, can be avoided [13]. The formation of NiO also causes a microstructural change, resulting in long-term cell degradation [14].

In general, the integration of the fuel cells leads to a complicated system involving many controlled and manipulated variables. Thus, the control design of integrated fuel cell systems is essential for efficient operation. There are many possible control structures for fuel cell systems. Xue et al. [15] successfully used a fuzzy fault-tolerance controller coupled with a Bayesian regularization neural network to control a SOFC with a reformer system; the SOFC system could be operated safely despite fluctuations in the steam feed flow rate. A linear-quadratic-Gaussian control was used to control a wind turbine-SOFC hybrid system, resulting in an increased system lifetime [16]. Chen et al. [17]

implemented six control loops to ensure the safe and effective operation of a SOFC-GT hybrid system with anode and cathode recirculation, in which the gas feed temperatures to the anode and cathode were controlled to avoid significant temperature differences and temperature gradients in the SOFC. This finding was also observed by Jienkulsawad et al. for a SOFC-MCFC integrated system [18]. A plantwide control configuration with an internal model control-based multi-loop control was successfully used to control the SOFC-GT hybrid system to meet the complete combustion, high power, lowest heat loss, and carbon dioxide emissions requirements [19]. A fuel cell system can be controlled to follow the load demand while achieving maximum efficiency point tracking by controlling the fuel consumption [20]. From literature reviews, most academic work has focused on stabilizing control and less on economic control. The control structure design procedure of Skogestad [21] considers both of these issues. With such a control structure design, Chatrattanawet et al. [22] simulated an economic control scheme for a standalone SOFC system. Jienkulsawad et al. [18]

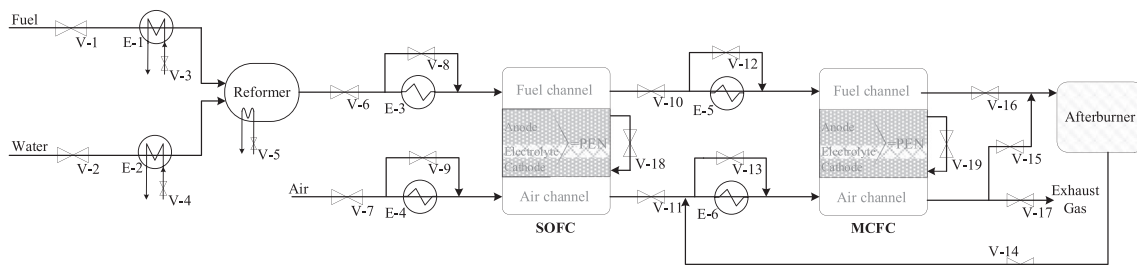


Fig. 1. Series configuration of the integrated SOFC-MCFC system.

performed a top-down analysis, the first half part of the control structure design procedure, of the integrated SOFC-MCFC system. The economic objective was to minimize the power generation costs and penalty costs of carbon dioxide emission (carbon tax) subjects to satisfying operational conditions; the self-optimizing controlled variables and throughput manipulator (TPM) were selected. Although suitable controlled variables from an economic point of view were identified in the previous work, a bottom-up analysis, the second part of the control structure design procedure, is necessary to validate whether the designed control structure can be efficiently implemented in practice.

The present work focuses on the bottom-up part of the plantwide control procedure, including the selection of manipulated variable (MV)-controlled variable (CV) pairings and the control configuration. The relative gain array (RGA) is used as a tool for selecting input-output pairings for decentralized control. Finally, the proposed control system is validated via dynamic simulations using Matlab.

## 2. Process description and models

A series configuration of the integrated SOFC-MCFC system is shown in Fig. 1. Methane (CH<sub>4</sub>) and steam (H<sub>2</sub>O) are fed as a hydrogen source to the reformer where the synthesis gas (e.g., carbon monoxide (CO), hydrogen (H<sub>2</sub>), and carbon dioxide (CO<sub>2</sub>)) generation takes place according to reactions (i) and (ii) in Table 1. A steam to methane molar feed ratio (S/C) of 2 is maintained to avoid carbon formation in the SOFC [23] and the reformer operates at 1 atm and 973 K. The synthesis gas is introduced to the SOFC anode, whereas air is fed to the SOFC cathode and reacts via electrochemical reactions (iii)–(v) in Table 1. Additional electric power is generated in the MCFC via reactions (vi)–(viii). The feed temperatures of the SOFC and MCFC were in a range of 973–1073 K and 823–873 K, respectively. The MCFC anode off-gas containing the remaining CO and H<sub>2</sub> is mixed with part of the cathode off-gas and burned in a combustion chamber to generate additional energy and concentrate the CO<sub>2</sub> before it is recirculated back to the cathode of the MCFC.

The fuel cell mathematical model (Table 2) includes mass and energy balances, as well as electrochemical models. Due to the high temperature, the radiation heat between the Positive-electrode (cathode)/Electrolyte/Negative-electrode(anode) (PEN) structure and interconnect (for connecting the neighboring cell) is included. The power generated by the fuel cells can be computed from the electrochemical part of the model, which relates the gas composition and temperature to the cell voltage (*E*) and current density (*j*). The mathematical model is based on the following assumptions: (1) pressure drop inside the channels is neglected, (2) heat loss to the surroundings is neglected, (3) all gases behave as ideal gases, (4) only hydrogen

oxidation is considered, and (5) complete combustion in the afterburner. The fuel cell models were validated with the experimental data from the literature in our previous study at various operating temperatures [24]. The fuel cell dimensions and electrochemical parameters are given in Tables 3 and 4.

## 3. Control structure design: Bottom-up analysis

The control structure design procedure of Skogestad [21] consists of two main parts; the top-down and the bottom-up part as outlined in Fig. 2. The main result from the top-down part (steps S1 to S4) is the selection of controlled outputs, mainly based on an economic steady-state optimization. From the previous study on the top-down analysis of the integrated SOFC-MCFC system (Fig. 1) [18], three active constraint regions (I, II, and III) as a function of the two main disturbances (fuel feed flowrate and steam feed flowrate) were identified. The normal operating point is in region I. Fortunately, the proposed set of eight controlled variables (CV1) in regions I and II are the same, as  $CV1 = [T_{of,S}, T_{oa,S}, y_{O_2,Moa}, y_{H_2,Mf}, T_{oa,M}, T_{f,M}/T_{of,M}, y_{H_2O,B0}, U_{f,M}]$ . Fuel utilization ( $U_{f,M}$ ) is not an active constraint in region I but the economic loss is small when  $U_{f,M}$  is kept constant at 75%. This implies that regions I and II can use the same control structure (Control structure A in [18]). This choice for CV1 is infeasible for region III due to the insufficient steam that is supplied to the system. However, feasibility is achieved when hydrogen at the MCFC anode outlet ( $y_{H_2,Mf}$ ) is replaced by hydrogen in the SOFC anode outlet ( $y_{H_2,Sf}$ ); this choice gives the smallest economic loss in region III. The electric power output, or more precisely, the MCFC current (V-19 in Fig. 1), was chosen as the throughput manipulator (TPM) because most of active constraints occur around the MCFC, indicating that it needs to be tightly controlled.

The bottom-up part (steps S5 to S7) deals with the design of the control system, including the selection of additional controlled outputs and pairings with manipulated inputs (valves V in Fig. 1). More details are given in the following sections.

### 3.1. Step S5. Structure of stabilizing control layer

The system should not drift too far from its acceptable operating point to ensure safe and stable operation. Among the 19 manipulated inputs (V-1–V-19 shown in Fig. 1), 8 inputs are used to control the economically controlled variables (CV1) found in the top-down part [18]. In addition, the MCFC current (V-19) is chosen as the TPM. The 10 remaining inputs are used to control 10 specified variables (CV2), including the steam to carbon ratio, temperatures, and pressures. Specifically, the set CV2 in this study is:

**Table 1**  
Chemical reactions.

Reformer	SOFC	MCFC	
*	*	*	Steam reforming reaction (SR) $CH_4 + H_2O \leftrightarrow 3H_2 + CO$ (i)
*	*	*	Water-gas-shift reaction (WGS) $CO + H_2O \leftrightarrow H_2 + CO_2$ (ii)
	*		Oxidation reaction (anode) $H_2 + O^{2-} \rightarrow H_2O + 2e^-$ (iii)
	*		Reduction reaction (cathode) $0.5O_2 + 2e^- \rightarrow O^{2-}$ (iv)
	*		Overall electrochemical reaction $H_{2,(an)} + 0.5O_{2,(ca)} \rightarrow H_2O_{(an)}$ (v)
		*	Oxidation reaction (anode) $H_2 + CO_3^{2-} \rightarrow H_2O + CO_2 + 2e^-$ (vi)
		*	Reduction reaction (cathode) $0.5O_2 + CO_2 + 2e^- \rightarrow CO_3^{2-}$ (vii)
		*	Overall electrochemical reaction $H_{2,(an)} + 0.5O_{2,(ca)} + CO_{2,(ca)} \rightarrow CO_{2,(an)} + H_2O_{(an)}$ (viii)

**Table 2**  
Summary of fuel cell models [18].

Mass balances (fuel and air channel)	
	$\frac{dN_i}{dt} \Big _{i \in \{\text{gaseous species}\}} = F_{0i} - F_i + \sum_j \nu_{i,j} \hat{R}_j A \quad (1)$
Energy balances	
Fuel Channel:	$\rho_f C_p V_f \frac{dT_f}{dt} = H_{0f} - H_f + Q_{P,f} + Q_{I,f} + \sum_{j \in \{(i),(ii)\}} (-\Delta H)_j \hat{R}_j A \quad (2)$
Air Channel:	$\rho_a C_p V_a \frac{dT_a}{dt} = H_{0a} - H_a + Q_{P,a} + Q_{I,a} \quad (3)$
PEN:	$\rho_p C_p V_p \frac{dT_p}{dt} = -Q_{P,f} - Q_{P,a} + Q_{rad} - IE + (-\Delta H)_{(v)} \hat{R}_{(v)} A \quad (4)$
Interconnect:	$\rho_I C_p V_I \frac{dT_I}{dt} = -Q_{I,f} - Q_{I,a} - Q_{rad} \quad (5)$
Enthalpy flow in/out	$H_k = \sum_i F_i \int_{298}^{T_k} C_{p,i} dT \quad (6)$
Heat conduction:	$Q_{j,k} = \frac{A k_k Nu (T_j - T_k)}{D_h} \quad (7)$
Heat radiation:	$Q_{rad} = A \left( \frac{\sigma (T_1^4 - T_2^4)}{1/\epsilon_j + 1/\epsilon_p - 1} \right) \quad (8)$
Electrochemical models	
Cell Voltage:	$E = E_{OCV} - \sum \eta_{loss} \quad (9)$
Current:	$I = jA \quad (10)$
Fuel Utilization:	$U_f = \frac{I}{2F(4F_{CH_4} + F_{CO} + F_{H_2})} \quad (11)$
SOFC:	Open-circuit voltage: $E_{OCV,S} = E^0 - \frac{\Re T}{2F} \ln \left( \frac{P_{H_2O}}{P_{H_2} P_{O_2}^{0.5}} \right) \quad (12)$
Concentration overpotentials:	$\eta_{con} = \frac{\Re T}{2F} \ln \left( \frac{P_{H_2O,TPB} P_{H_2,f}}{P_{H_2O,f} P_{H_2,TPB}} \right) + \frac{\Re T}{4F} \ln \left( \frac{P_{O_2,a}}{P_{O_2,TPB}} \right) \quad (13)$
Activation overpotentials:	$j = j_{0,an} \left[ \frac{P_{H_2,TPB}}{P_{H_2,f}} \exp \left( \frac{\alpha n F}{\Re T} \eta_{act,an} \right) - \frac{P_{H_2O,TPB}}{P_{H_2O,f}} \exp \left( -\frac{(1-\alpha)nF}{\Re T} \eta_{act,an} \right) \right] \quad (14)$
	$j = j_{0,ca} \left[ \exp \left( \frac{\alpha n F}{\Re T} \eta_{act,ca} \right) - \exp \left( -\frac{(1-\alpha)nF}{\Re T} \eta_{act,ca} \right) \right] \quad (15)$
Ohmic losses:	$\eta_{ohm} = j \sum_i \frac{\tau_i}{\sigma_i} \quad (16)$
MCFC:	Open-circuit voltage: $E_{OCV,M} = -\frac{\Delta G}{2F} - \frac{\Re T}{2F} \ln \left( \frac{P_{H_2O} P_{CO_2,f}}{P_{H_2} P_{O_2}^{0.5} P_{CO_2,a}} \right) \quad (17)$
Total losses:	$\sum \eta_{loss} = (R_{ir} + R_{an} + R_{ca})j \quad (18)$
Anode resistance:	$R_{an} = 2.04 \times 10^{-3} \exp \left( \frac{23.7}{\Re T} \right) P_{H_2}^{0.5} \quad (19)$
Cathode resistance:	$R_{ca} = 3.28 \times 10^{-9} \exp \left( \frac{132}{\Re T} \right) P_{O_2}^{-0.75} P_{CO_2}^{0.5} + 3.39 \times 10^{-6} \exp \left( \frac{67.1}{\Re T} \right) (2 \times 10^{-5} y_{H_2O} + y_{CO_2})^{-1} \quad (20)$
Electrolyte resistance:	$R_{ir} = 1.12 \times 10^{-2} \exp \left( \frac{23}{\Re T} \right) \quad (21)$

**Table 3**  
Fuel cell dimensions [24]

	SOFC	MCFC
Cell length, $L$ (m)	0.4	0.4
Cell width, $W$ (m)	0.1	0.8
Fuel channel height, $h_f$ (mm)	1	0.8
Air channel height, $h_a$ (mm)	1	0.8
Anode thickness, $\tau_{an}$ ( $\mu\text{m}$ )	500	-
Cathode thickness, $\tau_{ca}$ ( $\mu\text{m}$ )	50	-
Electrolyte thickness, $\tau_{el}$ ( $\mu\text{m}$ )	20	-
PEN thickness, $\tau_{PEN}$ ( $\mu\text{m}$ )	570	1000

**Table 4**  
Electrochemical parameters [24].

$\alpha$ (-)	0.5
$\sigma_{an}$ ( $\text{ohm}^{-1}\text{m}^{-1}$ )	$(9.5 \times 10^7/T) \exp(-1150/T)$
$\sigma_{ca}$ ( $\text{ohm}^{-1}\text{m}^{-1}$ )	$(4.2 \times 10^7/T) \exp(-1200/T)$
$\sigma_{el}$ ( $\text{ohm}^{-1}\text{m}^{-1}$ )	$33.4 \times 10^3 \exp(-10300/T)$
$\eta_{DC-AC}$ (%)	94

$$CV2 = [S/C, T_{CH_4}^0, T_{H_2O}^0, T_R, P_R, P_{f,S}, P_{a,S}, P_{f,M}, P_{a,M}, P_B]$$

The steam to carbon ratio (S/C) is controlled to avoid carbon formation in the SOFC. The temperatures are controlled to achieve the design conditions and avoid material stress in the fuel cells. The fuel cell voltage is also an important parameter but it is given indirectly from the hydrogen concentration and cell temperatures as reported in Chatrattanawet et al. (2015) [22]. The pressures represent gas holdups (inventory) and need to be controlled to achieve stable operation. The pairing of the pressure inventory loops follows the radiation rule [25] with the TPM located at the MCFC current (V-19).

Note that to simplify the model, the dynamics of these 10 loops are not included in the dynamic model, assuming adequate control in all pressure loops and considering all units are running at a constant pressure of 1 atm. Rather, these ten variables are specified in the model equations, which are all assumed to be static except for the fuel cell models (Table 2).

At this point, it is necessary to discuss the (dynamic) controllability of the system. To this effect, the locations of the poles and zeros are shown in Fig. 3. The poles and zeros are independent of the controller and control configuration and, therefore, reflect the controllability of the plant. Poles can tell whether the system is stable or not, whereas the

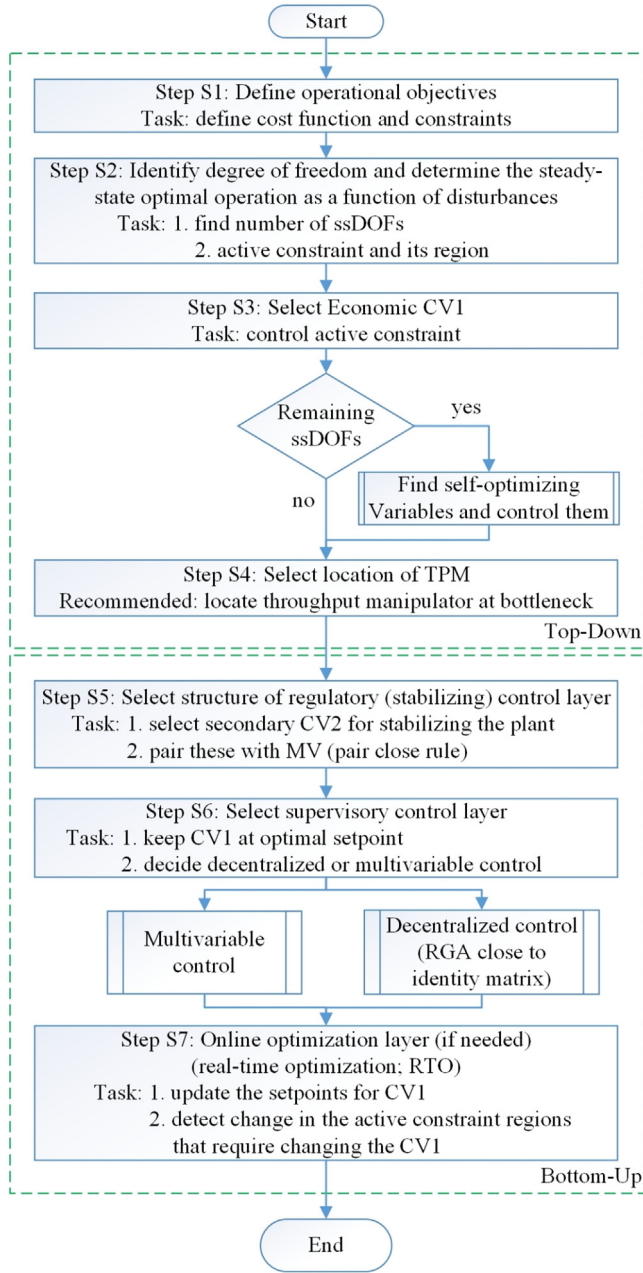


Fig. 2. Control structure design procedure.

zeros have an impact on the system’s transient characteristics. Unstable (RHP) zeros can imply serious control problems. Fig. 3 shows that all poles and zeros are stable (in LHP), so no particular problem is foreseen.

### 3.2. Step 6. Select supervisory control layer.

In this step, controllers are implemented to keep the eight economic controlled variables (CV1) at their optimal setpoints. Proportional-integral-derivative (PID) controllers are employed because they are common in industry, simple, cheap, and easy to implement. The control structure covering the normal operation (region I and II) is considered in this paper. Region III is considered the abnormal operation, happening when the fuel cell system has to increase the fuel feed and decrease the steam feed to reach the higher power demand without energy efficiency concerns. To avoid having the system cross to region III, a ratio controller is used to adjust the steam feed according to the methane feed (for controlling S/C in CV2). In total, with the TPM

located at V-19, 18 outputs (8 in CV1 and 10 in CV2) need to be controlled; therefore, identifying 18 pairings is required. The number of possible pairing combinations is very large ( $18! = 6.4 \times 10^{15}$ ). Fortunately, most of the pairings are obvious and can be decided by the “pair-close” rule (Rule 9 of Minasidis et al. [26]) and by the radiation rule around the TPM. For example, the temperatures on the six heat exchangers should be controlled by their respective bypass flows [27]. This removes pairing choices from the four temperatures in the CV1 set. In the following, the choice of pairings for the remaining four outputs in CV1 is considered.

$$CV1_C = [y_{O_2, M_{0a}}, y_{H_2O, B_0}, U_{f, M}, y_{H_2, M_f}]$$

These four variables involve composition measurements and are controlled on a relatively slow time scale so interactions between the loops can be significant. The other 14 variables are expected to be controlled locally on a fast time scale, so interactions will be much less. They are, in this analysis, assumed to be perfectly controlled, so pairing selection is not relevant. To control the four compositions in  $CV1_C$ , there are several choices for manipulated inputs.  $y_{O_2, M_{0a}}$  can be either controlled by valves V-7 or V-11.  $y_{H_2O, B_0}$  can be either controlled by V-15 or V-16.  $y_{H_2, M_f}$  can be either controlled by V-10 or V-18. The fuel utilization  $U_{f, M}$  is a function of the SOFC current density (V-18) and MCFC fuel feed (V-10), so it can be controlled by V-10 or V-18. Therefore, there are 6 possible MVs (V-6, V-7, V-10, V-11, V-15, and V-18) to control the four outputs in  $CV1_C$ . However, only the four combinations in Tables 5–8 need to be considered: V-15 and V-18 appear in all sets because they are needed to control either  $y_{H_2O, B_0}$ ,  $U_{f, M}$ , or  $y_{H_2, M_f}$ . V-6 and V-10 cannot appear in the same MV set because one of them is needed for pressure control. This argument also applies for V-7 and V-11.

As single-loop controllers (decentralized control) are implemented, input–output pairings are necessary; for this, the relative gain array (RGA) is a useful tool. The RGA of a non-singular square complex matrix (G) is given in Eq. (22), where  $\times$  denotes element by element multiplication.

$$RGA(G) = \Lambda(G) = G \times (G^{-1})^T \quad (22)$$

The steady-state RGA is shown for the four alternative MV sets in Tables 5 to 8. The main rule when using the steady-state RGA is to avoid pairing on negative RGA-elements; otherwise, the use of integral action adds instability if one of the loops is no longer active; for example, due to MV saturation. Based on this rule, there is only one possible pairing choice (shown in boldface) for each of the four MV sets.

In addition to avoiding negative RGA-elements, a value close to 1 is preferred for the selected pairings and with the other RGA-elements being close to 0. From this reasoning, MV set 2 in Table 6 comes out as the preferred choice with all paired RGA-elements close to 1. The resulting choice of pairings is then as follows for the set  $CV1_C$ : V-7 controls  $y_{O_2, M_{0a}}$ , V-15 controls  $y_{H_2O, B_0}$ , V-10 controls  $U_{f, M}$ , and V-18 controls  $y_{H_2, M_f}$ . This means that V-6 and V-11 will be used to control pressures in the fuel channel and air channel of the SOFC, respectively. The proposed pairings for all the 18 loops are shown in Fig. 4. The control loops in grey are for the set CV2. The control loops in red are the four temperature loops in  $CV1_T$ . Finally, the four control loops in blue are for remaining composition variables  $CV1_C$ . Note that in the simulations, only controllers for these last four loops are used. The remaining 14 variables in CV2 and  $CV1_T$  are assumed to be perfectly controlled, which means that the pairings indicated are not really implemented in the present simulations. This is reasonable since these 14 loops are expected to be much faster than the four loops for  $CV1_C$ .

## 4. Simulation of closed-loop performance

To verify that the system is controllable using single-loop PID control, the system was simulated for setpoint changes (Figs. 5 and 6) and



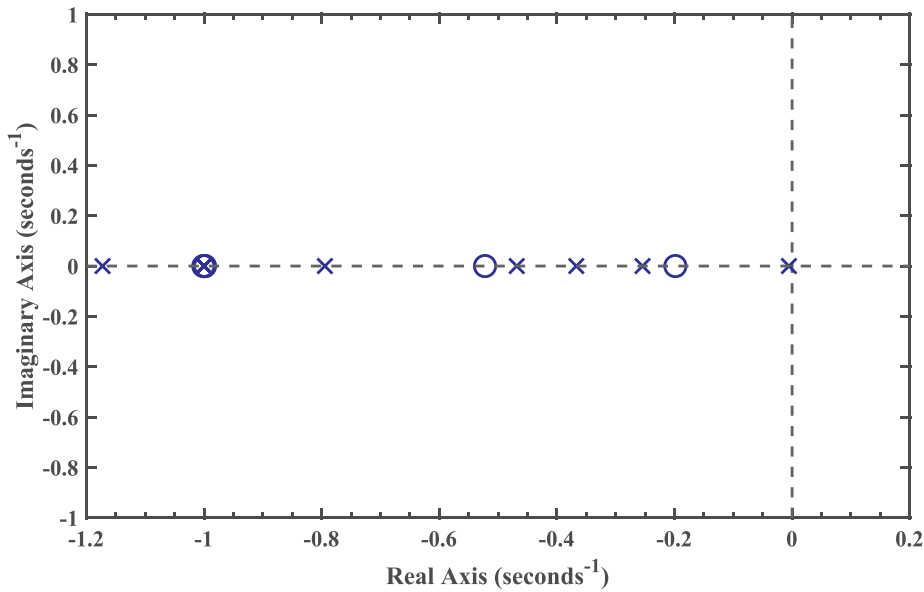


Fig. 3. Pole (x) and Zero (o) map of the dynamic model of the integrated system. There is an additional stable pole located at  $-11.2 \text{ s}^{-1}$ .

Table 5

RGA for CV1<sub>C</sub>: MV set 1.

	$F_{0f,S}(V-6)$	$F_{0a,S}(V-7)$	$F_{0a,B}(V-15)$	$I_S(V-18)$
$y_{O_2,M0a}$	0.0077	<b>0.9960</b>	-0.0040	0.0002
$y_{H_2O,B0}$	-0.0187	-0.0022	<b>1.0045</b>	0.0164
$U_{f,M}$	-4.3249	-0.0372	0.0000	<b>5.3621</b>
$y_{H_2,Mf}$	<b>5.3359</b>	0.0433	-0.0005	-4.3787

Table 6

RGA for CV1<sub>C</sub>: MV set 2.

	$F_{0a,S}(V-7)$	$F_{0f,M}(V-10)$	$F_{0a,B}(V-15)$	$I_S(V-18)$
$y_{O_2,M0a}$	<b>1.0030</b>	-0.0002	-0.0041	0.0013
$y_{H_2O,B0}$	-0.0036	-0.0038	<b>1.0121</b>	-0.0046
$U_{f,M}$	0.0012	<b>1.0987</b>	0.0000	-0.0999
$y_{H_2,Mf}$	-0.0005	-0.0947	-0.0079	<b>1.1032</b>

Table 7

RGA for CV1<sub>C</sub>: MV set 3.

	$F_{0f,S}(V-6)$	$F_{0a,M}(V-11)$	$F_{0a,B}(V-15)$	$I_S(V-18)$
$y_{O_2,M0a}$	-0.1029	<b>0.7574</b>	0.3343	0.0112
$y_{H_2O,B0}$	-0.0157	0.2061	<b>0.7956</b>	0.0140
$U_{f,M}$	-4.7440	0.0000	0.0000	<b>5.7440</b>
$y_{H_2,Mf}$	<b>5.8626</b>	0.0365	-0.1299	-4.7693

Table 8

RGA for CV1<sub>C</sub>: MV set 4.

	$F_{0f,M}(V-10)$	$F_{0a,M}(V-11)$	$F_{0a,B}(V-15)$	$I_S(V-18)$
$y_{O_2,M0a}$	0.0019	<b>0.6934</b>	0.3073	-0.0026
$y_{H_2O,B0}$	-0.0029	0.3070	<b>0.6992</b>	-0.0032
$U_{f,M}$	<b>1.0957</b>	0.0000	0.0000	-0.0957
$y_{H_2,Mf}$	-0.0946	-0.0004	-0.0065	<b>1.1015</b>

disturbances in current ( $I_M$ ) and feed rate (Figs. 7 and 8). The controlled outputs are shown in Figs. 5 and 7 and the manipulated inputs are shown in Figs. 6 and 8. In addition, Fig. 9 shows the resulting fuel cell voltages ( $E_S$  and  $E_M$ ) for the case with disturbances. The dynamic responses are shown in Figs. 5–9. The four PID controllers for controlling  $y_{O_2,M0a}$ ,  $y_{H_2O,B0}$ ,  $U_{f,M}$ , and  $y_{H_2,Mf}$  were tuned using the Skogestad internal model control (SIMC) tuning method, which is simple and works well on a wide range of processes [28]. To tune the controllers, a second-order model is first fitted for each of the four open-loops as:

$$g(s) = \frac{k}{(\tau_1 s + 1)(\tau_2 s + 1)} e^{-\theta s} \quad (23)$$

where  $k$  is the plant gain,  $\theta$  is the effective time delay,  $\tau_1$  is the dominant lag time constant, and  $\tau_2$  is the second-order lag time constant. The SIMC settings for a cascade form PID controller are:

$$K_c = \frac{1}{k} \frac{\tau_1}{\tau_c + \theta} \quad (24)$$

$$\tau_I = \min\{\tau_1, 4(\tau_c + \theta)\} \quad (25)$$

$$\tau_D = \tau_2 \quad (26)$$

$$C_{PID}(s) = \frac{K_c(\tau_I s + 1)(\tau_D s + 1)}{\tau_I s} \quad (27)$$

where  $\tau_c$  is the only tuning parameter. In this case, tight control is considered and thus,  $\tau_c = \theta$  is selected. The resulting PID settings are given in Table 9.

To evaluate the closed-loop performance, an integral absolute error (IAE) of the control error ( $e(t) = y^{SP} - y(t)$ ) was determined; the IAE should be as small as possible.

$$IAE = \int_0^\infty |e(t)| dt \quad (28)$$

#### 4.1. Setpoint changes

As seen in Figs. 5 and 6, all the dynamic responses are smooth according to the set-point changes shown in Table 10. Although the MV-CV pairings all have RGA-elements close to 1, there are some interactions. This is not surprising as, first, the RGA measures only two-way interactions and second, the RGA was obtained at steady-state conditions. Nevertheless, the interactions are quite small. At  $t_1$ , when the set point of  $y_{O_2,M0a}$  is increased, the first controller increases  $F_{0a,S}(V-7)$  as

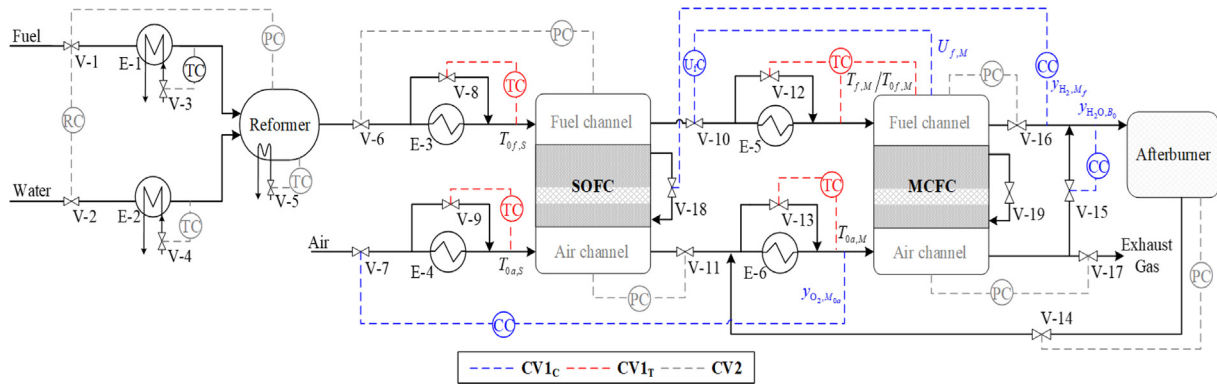


Fig. 4. Control structure A for regions I and II.

seen in Figs. 5 and 6. However, because of the interaction, the second controller has to reduce  $F_{O_2,B}$  (V-15) to keep  $y_{H_2O,B_0}$  constant. The main interaction is when a set-point change in  $U_{f,M}$  alone is made in  $t_6$  in Figs. 5 and 6. This results in some interactions with the other loops as the MV used to control  $U_{f,M}$ , which is  $V-10 = F_{of,M}$ , also affects the other CVs. Finally, note that at  $t_8$  when the set-point of  $y_{H_2,M_f}$  is decreased by 10%, the fourth controller increases the SOFC current  $I_s$  (V-18). This means that the SOFC anode-off gas will contain less fuel. This is akin to a reducing the fuel flow rate fed to MCFC resulting in the decrease of  $y_{H_2,M_f}$ .

#### 4.2. Disturbance changes

The disturbance responses in Figs. 7–9 are also smooth when the change is applied as given in Table 11. Several remarkable observations on these responses can be made. At time  $t_1$ , when the MCFC power

output ( $I_M$ ) is increased by 10%, the MCFC needs more fuel to generate more power so both feed rates (V-7 and V-10) increase. This results in a temporary drop in hydrogen at the MCFC anode outlet ( $y_{H_2,M_f}$ ) and a rise in the stream mole fraction in the burner ( $y_{H_2O,B_0}$ ). The oxygen at the MCFC cathode inlet ( $y_{O_2,Moa}$ ) is decreased initially because more  $O_2$  is used in the power generation and burning. Hence, all the controllers act at the same time.

#### 5. Discussion

The overall fuel cell system involves 18 control loops as shown in Fig. 4. However, as already mentioned, the dynamic simulations only include the four slowest loops (in blue in Fig. 4). The remaining 14 controlled outputs (CVs) are assumed as constant in the simulations (red and gray loops in Fig. 4). The justification for this is the time scale separation, that is, that these 14 loops are assumed to be significantly

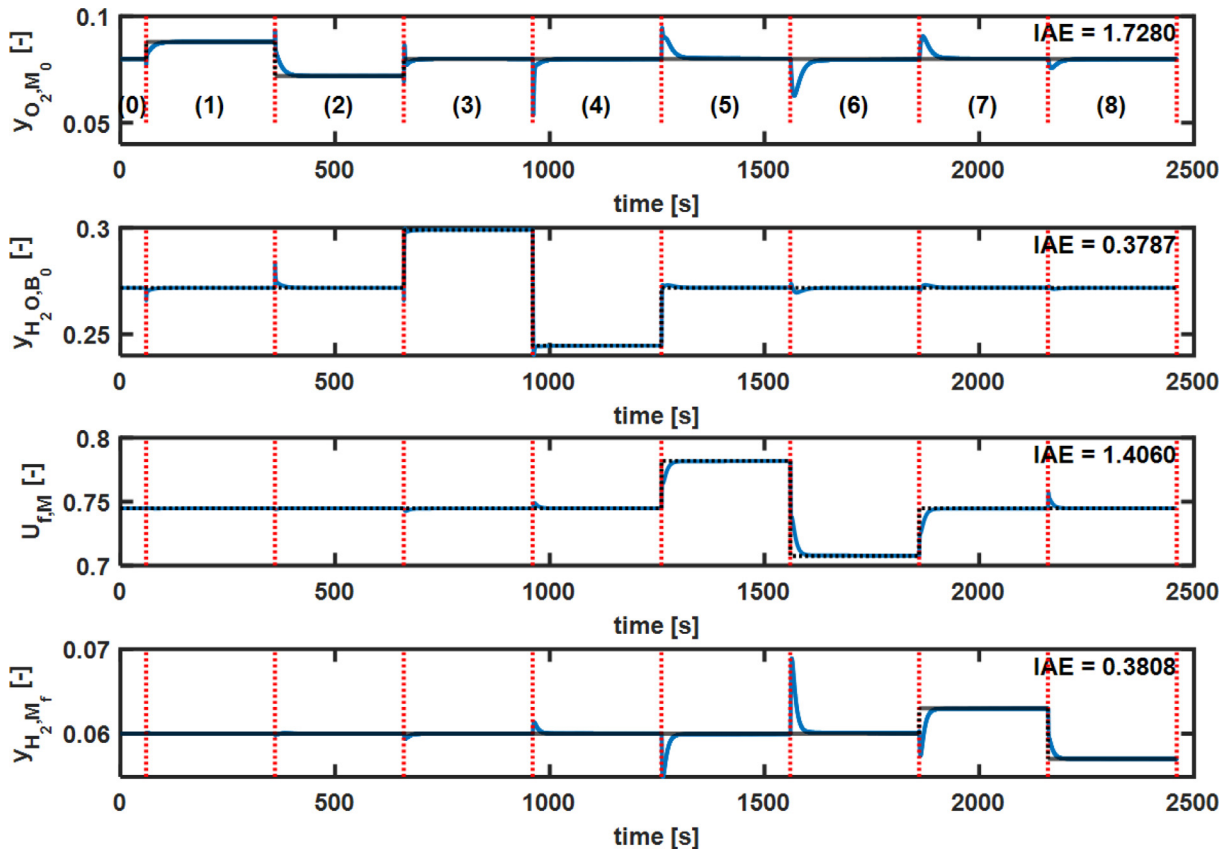


Fig. 5. Dynamic response of CV1c to set-point changes (Table 10).

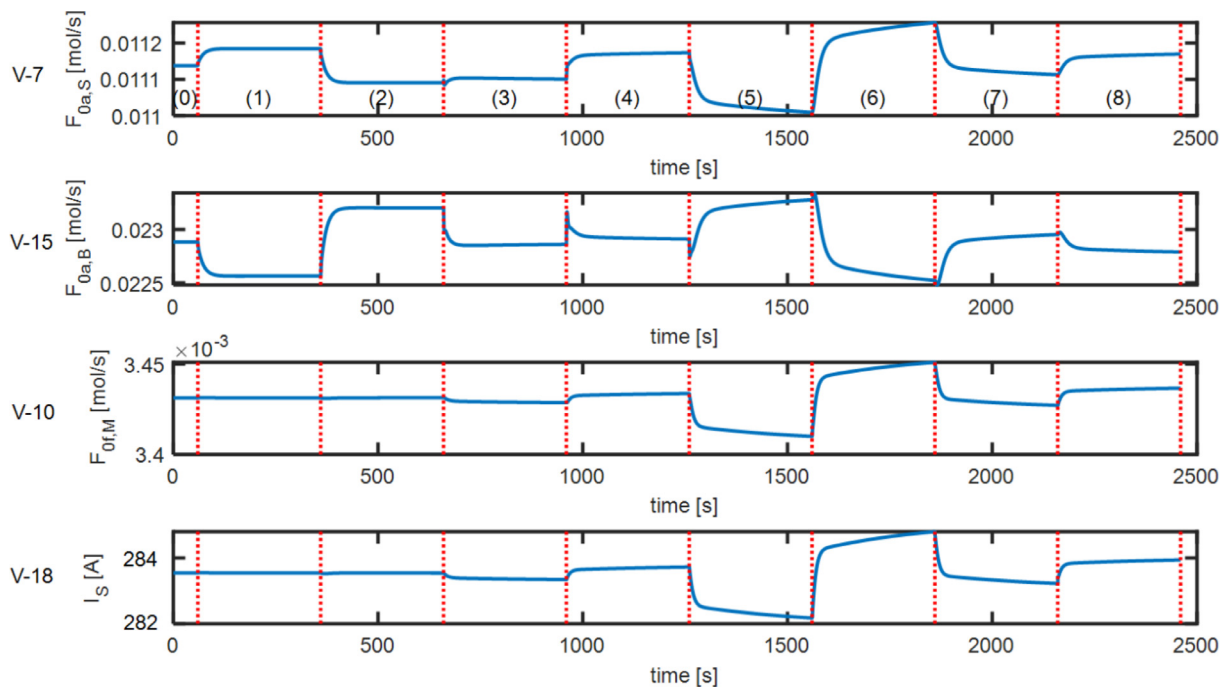


Fig. 6. Dynamic response of MVs to set-point changes (Table 10).

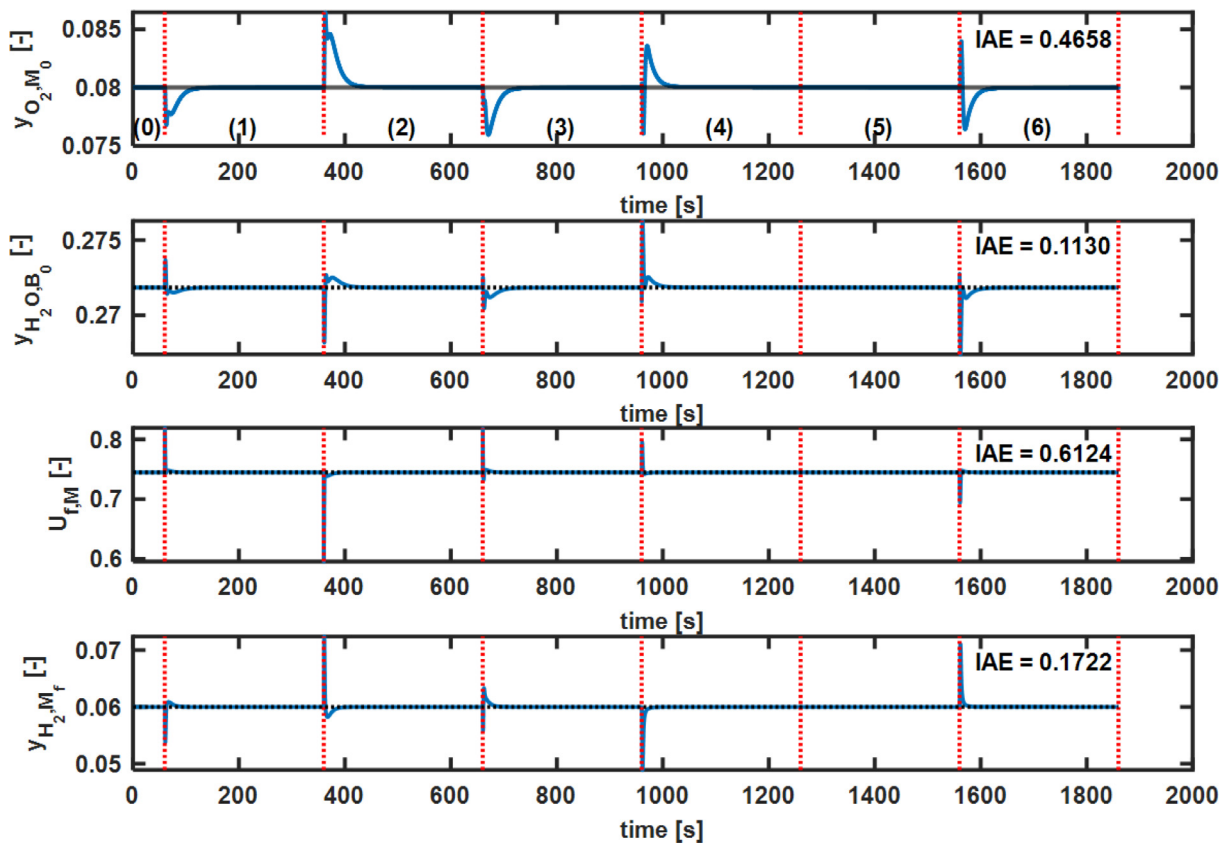


Fig. 7. Dynamic response of CV1C to disturbances (Table 11).

faster and can be considered to be constant within the slower time scale of the 4 slower loops. This introduces a small error, but it also greatly simplifies the dynamic model and tuning. Note that the fuel cell system is modeled in MATLAB and part of the model is steady state. This makes it possible to directly specify output variables, like temperatures and pressures.

The proposed control loops for the fuel cell system in this work are somewhat different from the control system proposed by other researchers [29]. Using the air flow rate is recommended to control the MCFC oxygen feed concentration instead of using it to control the temperature or fuel utilization. Similar to the work of Chatrattanawat et al. [22], control of the H<sub>2</sub> composition is essential to optimize



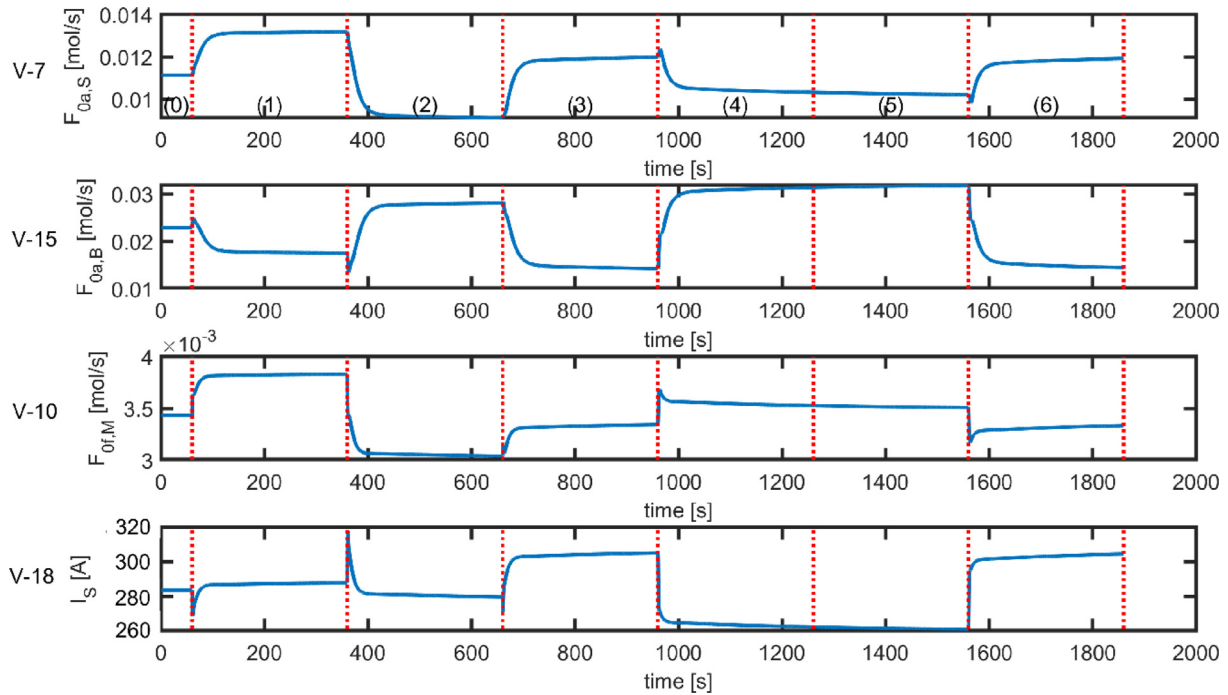


Fig. 8. Dynamic response of MVs to disturbances (Table 11).

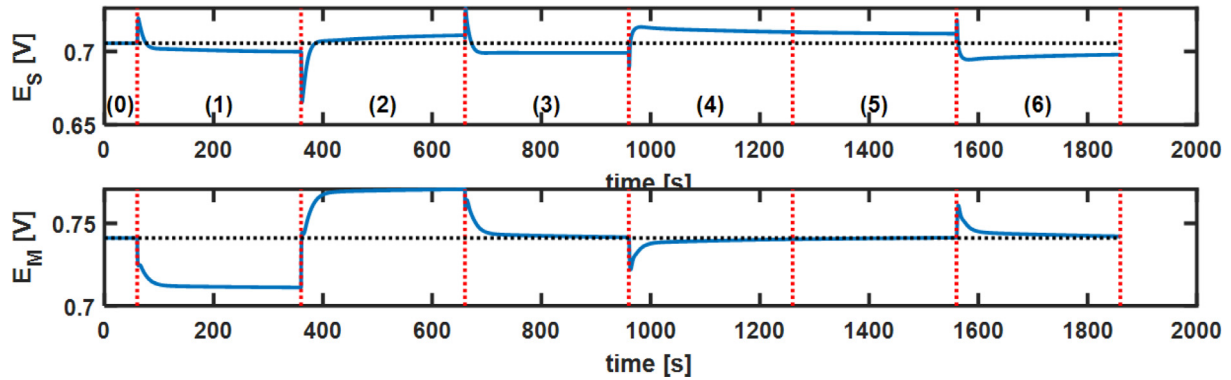


Fig. 9. Dynamic response of the uncontrolled fuel cell voltages to disturbances (Table 11).

Table 9  
PID controller parameters (cascade form).

	CV	$K_c$	$\tau_i$	$\tau_D$
1.	$y_{O_2,M0a}$	0.09	2.61	0.18
2.	$y_{H_2O,B0}$	-0.47	0.02	1.26
3.	$U_{f,M}$	-0.11	2.31	0.17
4.	$y_{H_2,Mf}$	$-3.11 \times 10^5$	3.91	1.52

economics. However, the following statement was found to not hold “When the hydrogen concentration and temperature are controlled, voltage will be indirectly controlled” [22]; the result of this study (Fig. 9) shows that this is not true for this system. The cell voltages cannot be controlled as they depend on the current, which is given by the operators and considered as a disturbance, and cell temperature. Although cell voltage cannot be controlled, it is still in the minimum allowance [30]. If the cell voltage needs to be controlled, for example if it drops too low, then the cell voltage would become the TPM. This should be easily implementable using a min-selector, for example.

Table 10  
Timetable for set-point changes.

Time (s)	Set-point change
$t_0 = 0$	Steady-state condition
$t_1 = 60$	$y_{O_2,M0a}$ is increased by 10%.
$t_2 = 360$	$y_{O_2,M0a}$ is decreased by 10% from the original set-point.
$t_3 = 660$	$y_{H_2O,B0}$ is increased by 10%. $y_{O_2,M0a}$ is changed back to its original.
$t_4 = 960$	$y_{H_2O,B0}$ is decreased by 10% from the original set-point.
$t_5 = 1260$	$U_{f,M}$ is increased by 10%. $y_{H_2O,B0}$ is changed back to its original.
$t_6 = 1560$	$U_{f,M}$ is decreased by 10% from the original set-point.
$t_7 = 1860$	$y_{H_2,Mf}$ is increased by 10%. $U_{f,M}$ is changed back to its original.
$t_8 = 2160$	$y_{H_2,Mf}$ is decreased by 10% from the original set-point

## 6. Conclusions

In this work, the second part of a control structure design based on Skogestad’s procedure was performed for a SOFC-MCFC integrated system. In the first part, controlled variables were proposed to achieve close-to-optimal power generation while reducing carbon dioxide emissions and achieving safe operation [18]. In the second part, it was

**Table 11**  
Timetable for disturbances changes.

Time (s)	Disturbance changes
$t_0 = 0$	Steady-state condition
$t_1 = 60$	MCFC current $I_M$ (V-19) increased by 10%.
$t_2 = 360$	MCFC current $I_M$ (V-19) decreased by 10% from its original value.
$t_3 = 660$	Methane feed flow rate (V-1) increased by 10%. MCFC current $I_M$ (V-19) shifted to its original value.
$t_4 = 960$	Methane feed flow rate (V-1) decreased by 10% from its original value.
$t_5 = 1260$	Steam feed flow rate (V-2) increased by 10%. Methane feed flow rate (V-1) shifted to its original value.
$t_6 = 1560$	Steam feed flow rate (V-2) decreased by 10% from its original value.

confirmed that this system is indeed controllable. The overall fuel cell system has 18 control loops (Fig. 4) but because of the time scale separation between the regulatory layer and slower supervisory layer, only four slower composition loops were included in the dynamic simulation. The remaining 14 controlled outputs were assumed as constant in the simulation. RGA-analysis, used to select appropriate pairing of these four loops, and dynamic simulation of the fuel-cell system show that smooth responses can be achieved using simple single-loop PID controllers. The cell voltages deviated from their normal values, which were not controlled in our work.

#### CRedit authorship contribution statement

**Prathak Jienkulsawad:** Methodology, Software, Validation, Writing - original draft. **Sigurd Skogestad:** Conceptualization, Visualization, Writing - review & editing. **Amornchai Arpornwichanop:** Conceptualization, Methodology, Supervision, Funding acquisition, Writing - review & editing.

#### Declaration of Competing Interest

The authors declare that they have no known competing financial interests or personal relationships that could have appeared to influence the work reported in this paper.

#### Acknowledgments

The support of the Chulalongkorn Academic Advancement into its 2nd Century Project (Chulalongkorn University) and the Royal Golden Jubilee Ph.D. Program (Thailand Science Research and Innovation) is gratefully acknowledged.

#### References

- [1] Kupecki J, Skrzypkiewicz M, Motylinski K. Variant analysis of the efficiency of industrial scale power station based on DC-SOFCs and DC-MCFCs. *Energy* 2018;156:292–8.
- [2] Chelmehsara ME, Mahmoudimehr J. Techno-economic comparison of anode-supported, cathode-supported, and electrolyte-supported SOFCs. *Int J Hydrogen Energy* 2018;43:15521–30.
- [3] Palomba V, Ferraro M, Frazzica A, Vasta S, Sergi F, Antonucci V. Experimental and numerical analysis of a SOFC-CHP system with adsorption and hybrid chillers for telecommunication applications. *Appl Energy* 2018;216:620–33.
- [4] Mehrpooya M, Sadeghzadeh M, Rahimi A, Pouriman M. Technical performance analysis of a combined cooling heating and power (CCHP) system based on solid oxide fuel cell (SOFC) technology – a building application. *Energy Convers Manage* 2019;198:111767.
- [5] Wu Z, Zhu P, Yao J, Tan P, Xu H, Chen B, et al. Thermo-economic modeling and analysis of an NG-fueled SOFC-WGS-TSA-PEMFC hybrid energy conversion system for stationary electricity power generation. *Energy* 2020;192:116613.
- [6] Vialeto G, Noro M, Colbataldo P, Rokni M. Enhancement of energy generation efficiency in industrial facilities by SOFC – SOEC systems with additional hydrogen production. *Int J Hydrogen Energy* 2019;44:9608–20.
- [7] Bessekou Y, Zielke P, Wulff AC, Hagen A. Simulation of a SOFC/Battery powered vehicle. *Int J Hydrogen Energy* 2019;44:1905–18.
- [8] Wu Z, Tan P, Zhu P, Cai W, Chen B, Yang F, et al. Performance analysis of a novel SOFC-HCCI engine hybrid system coupled with metal hydride reactor for H<sub>2</sub> addition by waste heat recovery. *Energy Convers Manage* 2019;191:119–31.
- [9] Ehyaei MA, Rosen MA. Optimization of a triple cycle based on a solid oxide fuel cell and gas and steam cycles with a multiobjective genetic algorithm and energy, exergy and economic analyses. *Energy Convers Manage* 2019;180:689–708.
- [10] Wu Z, Ni M, Zhu P, Zhang Z. Dynamic modeling of a NG-fueled SOFC-PEMFC hybrid system coupled with TSA process for fuel cell vehicle. *Energy Procedia* 2019;158:2215–24.
- [11] Jienkulsawad P, Saebaa D, Patcharavorachot Y, Arpornwichanop A. Performance assessment of a hybrid solid oxide and molten carbonate fuel cell system with compressed air energy storage under different power demands. *Int J Hydrogen Energy* 2020;45:835–48.
- [12] Nehter P. A high fuel utilizing solid oxide fuel cell cycle with regard to the formation of nickel oxide and power density. *J Power Sources* 2007;164:252–9.
- [13] Jienkulsawad P, Saebaa D, Patcharavorachot Y, Kheawhom S, Arpornwichanop A. Analysis of a solid oxide fuel cell and a molten carbonate fuel cell integrated system with different configurations. *Int J Hydrogen Energy* 2018;43:932–42.
- [14] Parhizkar T, Roshandel R. Long term performance degradation analysis and optimization of anode supported solid oxide fuel cell stacks. *Energy Convers Manage* 2017;133:20–30.
- [15] Xue T, Wu X, Zhao D, Xu Y, Jiang J, Deng Z, et al. Fault-tolerant control for steam fluctuation in SOFC system with reforming units. *Int J Hydrogen Energy* 2019;44:23360–76.
- [16] Yu D, Mao Y, Gu B, Nojavan S, Jermisittiparsert K, Nasser M. A new LQG optimal control strategy applied on a hybrid wind turbine/solid oxide fuel cell/ in the presence of the interval uncertainties. *Sustainable Energy Grids Networks* 2020;21:100296.
- [17] Chen J, Liang M, Zhang H, Weng S. Study on control strategy for a SOFC-GT hybrid system with anode and cathode recirculation loops. *Int J Hydrogen Energy* 2017;42:29422–32.
- [18] Jienkulsawad P, Skogestad S, Arpornwichanop A. Control structure design of a solid oxide fuel cell and a molten carbonate fuel cell integrated system: top-down analysis. *Energy Convers Manage* 2017;152:88–98.
- [19] Wu W, Chen S-A, Hwang J-J, Hsu F-T. Optimization and control of a stand-alone hybrid solid oxide fuel cells/gas turbine system coupled with dry reforming of methane. *J Process Control* 2017;54:90–100.
- [20] Bizon N, Oproescu M, Raceanu M. Efficient energy control strategies for a stand-alone renewable/fuel cell hybrid power source. *Energy Convers Manage* 2015;90:93–110.
- [21] Skogestad S. Control structure design for complete chemical plants. *Comput Chem Eng* 2004;28:219–34.
- [22] Chatrattanawet N, Skogestad S, Arpornwichanop A. Control structure design and dynamic modeling for a solid oxide fuel cell with direct internal reforming of methane. *Chem Eng Res Des* 2015;98:202–11.
- [23] Adams TA, Nease J, Tucker D, Barton PI. Energy conversion with solid oxide fuel cell systems: a review of concepts and outlooks for the short- and long-term. *Ind Eng Chem Res* 2013;52:3089–111.
- [24] Jienkulsawad P, Arpornwichanop A. Investigating the performance of a solid oxide fuel cell and a molten carbonate fuel cell combined system. *Energy* 2016;107:843–53.
- [25] Aske EMB, Skogestad S. Consistent inventory control. *Ind Eng Chem Res* 2009;48:10892–902.
- [26] Minasidis V, Skogestad S, Kaistha N. Simple rules for economic plantwide control. *Comput Aided Chem Eng* 2015;37:101–8.
- [27] Escobar M, Trierweiler JO. Bypass design for control and optimization of heat exchanger networks. *Computer Aided Chem Eng* 2009;27:1665–70.
- [28] Skogestad S. Simple analytic rules for model reduction and PID controller tuning. *J Process Control* 2003;13:291–309.
- [29] Huang B, Qi Y, Murshed M. Solid oxide fuel cell: perspective of dynamic modeling and control. *J Process Control* 2011;21:1426–37.
- [30] Aguiar P, Adjiman C, Brandon N. Anode-supported intermediate temperature direct internal reforming solid oxide fuel cell: II. Model-based dynamic performance and control. *J Power Sources* 2005;147:136–47.